CO6-1 Structural study of the overlapping tri-nucleosome in solution

M. Nishimura[1], K. Nozawa[1], K. Morishima[2], R. Inoue[2], M. Sugiyama[2], and H. Kurumizaka[1]

[1]*Laboratory of Chromatin Structure and Function, Institute for Quantitative Biosciences, The University of Tokyo*

[2]*Institute for Integrated Radiation and Nuclear Science , Kyoto University(KURNS)*

INTRODUCTION:

In eukaryote, the genomic DNA is organized hierarchically into chromatin structures, and is stored in the nucleus. The basic unit of chromatin is the nucleosome, in which approximately 145 base-pairs of DNA are wrapped around the histone octamer containing two molecules of each core histone, H2A, H2B, H3, and H4. Emerging evidence suggests that the chromatin includes diverse repertoire of basic structural units [1]. Our group previously reported the three-dimensional structure of an overlapping dinucleosome: OLDN, which is an intermediate structure formed when two nucleosomes collide and release one H2A-H2B dimer in chromatin [2]. In the OLDN structure, the octameric histone core and the hexameric histone core are intimately associated each other, and 250 base-pairs of DNA are continuously wrapped around it. Assuming that the OLDN forms a further higher-order complex, we prepared an overlapping tri-nucleosome; OLTN, in which one octameric histone core and two hexameric histone cores are intimately associated, and approximately 350 bp DNAs are wrapped around the core. In this study, we analyzed the solution structure of the canonical nucleosome, OLDN, and OLTN by small-angle X-ray scattering (SAXS) and analytical ultracentrifuge (AUC).

EXPERIMENTS:

To generate OLTN, we prepared a DNA fragment with tandemly arranged three nucleosome positioning sequences derived from the Widom 601 sequence in a 353 bp fragment. The canonical nucleosome, OLDN, and OLTN were reconstituted by the salt dialysis method with recombinant human histones and DNAs, as previously described [2]. The reconstituted nucleosomes were purified by non-denaturing gel electrophoresis. SAXS analyses were performed with a NANOPIX instrument (RIGAKU) at the Institute of Radiation and Nuclear Science, Kyoto University. In order to cover the wide *q*-range, we employed two sample-to-detector distance: 1,330 mm and 350 mm, and then combined these data. We also performed the standard procedures of transmission correction, buffer solution scattering subtraction, and conversion to an absolute scale with water scattering. Nucleosome samples for SAXS included slight aggregates. To correct for the scattering data from those aggregates, we then performed AUC and corrected the SAXS data as previously described [3].

RESULTS:

We obtained the SAXS curves of the canonical nucleosome, OLDN, and OLTN, and the values of the radius of gyration (*Rg*) were calculated. As results, the *Rg* values of the nucleosome, OLDN, and OLTN were calculated as 43.6, 57.0, and 70.1, respectively [Fig.1]. However, the estimated molecular weight from the scattering intensity at the origin, was significantly lower than that from DNA sequence and histone amino acid sequence, implying that the OLTN solution include aggregates. The subsequent AUC experiment revealed that the nucleosome and OLDN samples resulted almost a monodispersed peak. On the other hand, the OLTN sample was separated by several peaks, suggesting that the OLTN solution contained aggregates. We then recalculated the SAXS profile by removing the portion corresponding to aggregates. We finally examined the OLTN structure by generating ab initio 3D-modeling from the corrected SAXS profile, followed by NMA refinements. The result revealed that the solution structure of OLTN is likely to be the octasome-hexasome-hexasome arrangement, but not the hexasome-octasome-hexasome structure [Fig. 2].

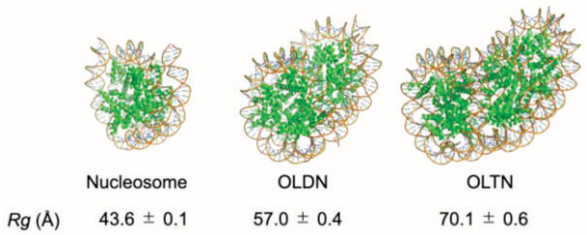

Fig.1 The *Rg* values of the nucleosome, OLDN, and OLTN in derived from SAXS-AUC analysis

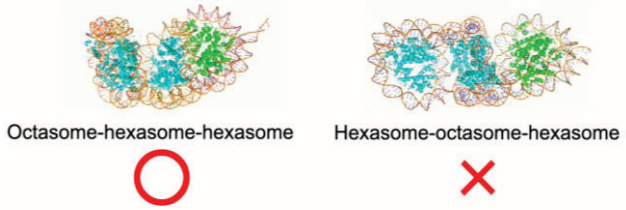

Fig.2 The schematic representations of the putative solution structures of OLTN.

REFERENCES:

[1] M. Koyama and H. Kurumizaka, J. Biochem. **163** (2018) 85-95.
[2] D. Kato *et al*., Science. **356** (2017) 205-208.
[3] K. Morishima *et al*., Commun. Biol. **3** (2020) 294.

CO6-2 Character of DNA damage induced by nuclear palnt neutron beams

H. Terato, T. Hanafusa, M. Isobe, M. Takigawa[1], S. Ihara[2], K. Mori[3], Y. Tokuyama[3], Y. Sakurai[4], and T. Saito[4]

Advanced Science Research Center, Okayama University

[1]Graduate School of Medicine, Dentistry, and Pharmceutical Sciences, Okayama University

[2]Graduate School of Engineering, Saga University

[3]Analytical Research Center for Experimental Sciences, Saga University

[4]KURNS

INTRODUCTION: Ionizing radiation takes severe biological consequences such as respective acute and chronic effects. These effects are usually arrived via the DNA damaging, because DNA brings the genetic information. Radiation DNA damage are produced by direct and indirect effects of ionizing radiation. Ionizing radiation attack DNA directly and via the generated reactive oxygen species (ROS) in direct and indirect effect pathways. We have had a lot of studies for radiation DNA damage after the discovery of X-rays by WC Roentgen in 1895. But the most of these studies have been derived from X-rays and gamma-rays, because we had not certain procedures to deliver the various ionizing radiation. Therefore, we have studied for the DNA damage with heavy ion beams, previously [1, 2]. These studies indicated that the DNA damage with heavy ion beams were unique, indicating that a lot of clustered DNA damage were generated including DNA double strand break (DSB), clustered base lesions, and these mixtures. Clustered DNA damage is a complex damage containing multiple lesions in the local region of DNA. This damage is mainly produced by the direct effect and highly concentrated ROS with heavy ion beam. This damage can inhibit DNA polymerization with high efficiently stopping of DNA polymerase moving on DNA. Also, this damage shows less repairable.

Neutron beam also shows severe biological damage like heavy ion beams, but the mechanism showing the consequence have not been unveiled yet. Thus, we analyze the DNA damage with neutrons from nuclear power plant to unveil the molecular mechanism of neutron biological effect in this study. The neutron beam is also high LET radiation as same as heavy ion beam. Therefore, we will find some interesting character of DNA damage with neutron like heavy ion beam. In the previous study periods, we found the relatively higher yields of DNA damage with the neutron beams than gamma-rays. In this year, we repeated DNA damage estimation for the result accuracy assurance, and investigated the cell effect for the neutron beams for the biological effect of this radiation.

EXPERIMENTS: Cultured cells of Chinese hamster ovary (CHO) AA8 strain were irradiated with neutron beams in the Kyoto University Reactor. The cells were cultivated with the conventional method. The logarithmic growing cells were recovered by trypsinization, and set into a polypropylene tube for irradiation. The estimated dose rate of neutron was 1Gy h^{-1}. The irradiated cells extracted in every 30 minutes up to 3 hours. After irradiation, the cells were immediately dissolved again with the cultured medium and reseeded into fresh medium. The cells were cultivated for 10 days for growing the colony. The colony was fixed with ethanol and stained with methylene blue. The colony number was counted for estimation of the irradiated cell viability. Simultaneously a half of the sampled cells were analyzed by agarose gel electrophoresis for DNA damage estimation. In DNA damage analysis, the irradiated cells were immediately frozen and stored at -80°C until the analysis. The frozen cells were embedded in low melting agarose plug and treated by protease. Then the plugs were subjected by electrophoresis.

RESULTS AND DISCUSSION: The sensitivity of the cells to neutron radiation increased in a dose-dependent manner. The increase in sensitivity was linear with dose, similar to radiosensitivity with other ionizing radiation species. On the other hand, the degree of sensitivity with D_{37} being 0.35 Gy was larger for gamma-rays and X-rays. The D_{37} is 1/10 of that of gamma-rays, and is consistent with the high biological effects of neutron radiation as well as other high-LET radiation. The dosimetry of the neutrons indicates that a half of dose of the reactor neutrons is derived from the contaminated gamma-rays. Gamma-rays usually show that the D_{37} is around 4 Gy. This result suggests that the neutron has greater efficiency for the biological effect. We already have the result indicating that the neutron showed relatively higher efficiency to generate the DNA damage than gamma-rays. Thus, the severe biological effect with neutron beam seems to be derived from the higher yield of DNA damage. The result of the cell viability is also consistent with the high DNA damage yield of neutron radiation obtained in the previous and this years' results. The results showed low yields of DSBs, which are considered to be directly related to cell survival, unlike other high-LET radiation. Therefore, it is necessary to clarify the DNA damage species involved in the high sensitivity to neutron radiation.

REFERENCES:

[1] H. Terato et al., J. Radiat. Res., 49 (2008) 133-146.
[2] Y. Tokuyama et al., J. Radiat. Res., 56 (2015) 446-455.

CO6-3

Evaluation of radiation resistance of lens constituent proteins involved in age-related cataract

T. Takata[1] and K. Lampi[2]

[1] *Institute for Integrated Radiation and Nuclear Science, Kyoto University*
[2] *Oregon Health & Science University*

INTRODUCTION:

The transparency and high refraction of the lens are maintained by the stable long-lived protein interactions, comprising α-, β-, and γ-crystallin families. As exposed outside body tissues, various damages of lens protein, such as oxidative damage, is increased during life. The lens contains various protection systems to prevent oxidative stress; however, damaged proteins can still accumulate because these protection systems are lost with aging, and there is no protein turnover or exclusion system in the lens. The damaged proteins include human lens crystallins that have been further subjected to the oxidation of amino acid residues [1].

These modifications, which are generated by UV light, ionizing irradiation and oxidative stress, decrease lens transparency and ultimately lead to the development of age-related cataracts [2, 3]. There are many data on the oxidation "sites" of aged human lens crystallins, but there are few studies of the oxidation "effects" of modification of amino acid in each crystallin species that have been subjected to γ-irradiation. γ-Irradiation generates free radicals and reactive oxygen species (ROS) such as hydroxyl radicals, superoxide, and singlet oxygen, which have been predicted to induce the oxidation of amino acids, as well as the truncation and cross-linking of proteins.

The aim of this study was to identify the effect of oxidation that occur in recombinantly expressed lens βB2-crystallin irradiated with low-dose γ-rays. The irradiated human lens βB2-crystallin (recombinantly expressed in *E. coli*) were loaded into reducing SDS-PAGE or digested by trypsin. The resulting peptides were analyzed by LC–MS/MS to identify the specific sites of oxidation in βB2-crystallin.

EXPERIMENTS:

Material Recombinantly lens βB2-crystallin were prepared and purified as described previously [4].

Gamma-irradiation βB2-crystallin, dissolved in 50 mM sodium phosphate buffer (pH 7.4), 150 mM NaCl were irradiated with γ-rays at a dose of 5, 50 or 500 Gy. γ-Irradiation was carried out at the Co-60 Gamma-ray Irradiation Facility of the Kyoto University Research Reactor Institute.

SDS-PAGE of Irradiated lens βB2-crystallin Each sample after irradiation was suspended in 50 μl of Laemmli SDS sample buffer (50 mM Tris-HCl, pH 6.8, 100 mM dithiothreitol, 2% SDS, 10% glycerol and 0.1% bromphenol blue). Each sample were loaded into 10% poly-acrylamide gel, then stained with coomassie brilliant blue to visualize the abnormal size oligomer.

LC-MS analysis Peptides from irradiated βB2-crystallins were obtained by in-gel digestion. The extracted tryptic peptides were filtered and injected into LC-MS/MS for modification analysis as previously reported [5]. Each sample was eluted over 60 min with a linear gradient (5%–45%) formed by mixing solvent A (0.1% formic acid aqueous solution) and solvent B (100% acetonitrile containing 0.1% formic acid). The oxidation was screened using by Proteome Discoverer™ 1.0 software (ThermoFisher, USA).

RESULTS:

Dose-dependent increasing size of βB2-crystallin after irradiation was observed (Fig. 1). The dimeric band was increased with decreased monomeric band of βB2-crystallin. The reason for the dimer formation was obscured, under the reducing situation during electrophoresis. Abnormal cross-linking molecules, such as tyrosine cross-linking, would be involved. There was also presenting truncated βB2-crystallin after irradiation. The band pattern was not ladder state, but suggested distinct state, thus this truncation would be site-specific in βB2-crystallin. LC-MS/MS analysis detected the oxidation of some tryptophan residues (W58, W150) on the βB2-crystallin after irradiation. Both sites have been previously reported, but still unknown the effect of modification. Further experiments to investigate the modification effect to induce abnormal aggregate using with mimic βB2-crystallin protein.

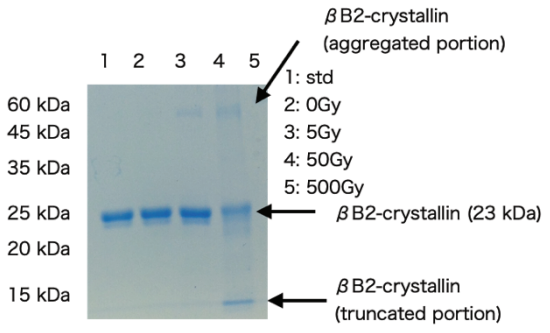

Fig. 1. Reducing SDS-polyacrylamide gel electrophoresis for irradiated βB2-crystallin.

REFERENCES:

[1] B. Searle *et al.*, *J Proteome Res*, **4** (2005) 546-554.
[2] S. Cai *et al.*, *Free Radic Biol Med.* **65** (2013) 1037-1046.
[3] E. C. Finley *et al.*, *Photochem Photobiol.* **68** (1998) 9-15.
[4] K. Lampi *et al.*, Biochemistry. **45** (2006) 3146-3153.
[5] T. Takata *et al.*, *FEBS Lett.* **285** (2018) 2263-2277.

CO6-4 A feasibility study of inverse contrast-matching small-angle neutron scattering method combined with size exclusion chromatography using antibody interactions as model systems

M. Yagi-Utsumi, K. Kato, S. Yanaka, R. Yogo, N. Sato[1], K. Morishima[1], R. Inoue[1], and M. Sugiyama[1]
Exploratory Research Center for Life and Living Systems (ExCELLS) and Institute for Molecular Science (IMS), National Institutes of Natural Sciences
[1]*Institute for Integrated Radiation and Nuclear Science, Kyoto University*

INTRODUCTION: Small-angle neutron scattering (SANS) and small-angle X-ray scattering (SAXS) are powerful techniques for the structural characterization of biomolecular complexes. In particular, SANS enables a selective observation of specific components in complexes by selective deuteration with contrast-matching techniques. In most cases, however, biomolecular interaction systems with heterogeneous oligomers often contain unfavorable aggregates and unbound species, hampering data interpretation. To overcome these problems, SAXS has been recently combined with size exclusion chromatography (SEC), which enables the isolation of the target complex in a multi-component system. By contrast, SEC–SANS is only at a preliminary stage. Hence, we herein perform a feasibility study of this method based on inverse contrast-matching (iCM) SANS technique using antibody interactions as model systems.

EXPERIMENTS: We perform a feasibility study of SEC–iCM–SANS using antibody interactions as models. Namely, immunoglobulin G (IgG) or its Fc fragment was mixed with 75% deuterated Fc-binding proteins, i.e. IgG-degrading enzyme of *Streptococcus pyogenes* (IdeS) and a soluble form of Fcγ receptor IIIb (sFcγRIIIb, hereafter referred to simply as FcγR). SEC–SAXS measurements were performed at 25°C with the La-SSS system installed into the laboratory-based SAXS instruments (NANOPIX, Rigaku). SEC–SANS measurements were conducted with a SEC–SANS system equipped with instrument D22 of ILL (Fig.1).

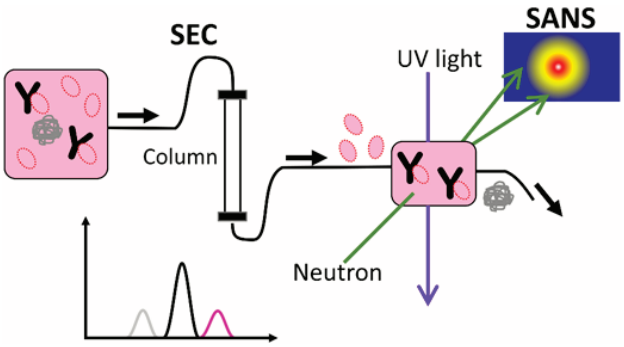

Fig. 1. Schematic illustration of SEC–iCM–SANS. The target complex can be selectively observed excluding the higher molecular weight aggregates and unbound species.

RESULTS: We attempted to apply the SEC–iCM–SANS method to the larger IgG–FcγR interaction system. A 1:1 mixture of IgG and FcγR was subjected to the SEC–SANS system and SEC–SAXS as a reference. In both systems, SEC enabled the selective acquisition of scattering data of free Fc and IgG–FcγR complex (Fig. 2). The FcγR-bound IgG had smaller R_g values (50.4 ± 1.4 Å in SAXS and 47.9 ± 1.9 Å in SANS) than those obtained for free IgG (54.9 ± 1.5 Å in SAXS and 52.0 ± 1.9 Å in SANS). We also measured the SEC–SANS profile of the complex formed with dFcγR and non-deuterated IgG, thereby providing the R_g value of IgG in the complex as 53.4 ± 1.7 Å, which was equivalent with the R_g value of free IgG due to the reasonably unobservable FcγR. In general, R_g becomes larger when the molecules form a complex. It should be noted, however, that R_g rather reduces upon complex formation when the inner space of the molecule is filled with another molecule, further resulting in an increased mass density around the original gravity center. The apparent recovery of the R_g value in the iCM–SANS observed with 75% deuterated FcγR as "transparent" binding partner is consistent with the above explanation. Indeed, the crystal structures of Fc in complex with FcγR (or its homologous sFcγRIIIa) have revealed that the receptor binding is carried primarily by the hinge-proximal part in Fc, which corresponds to the nearly central part in the intact IgG molecule.

The SEC–iCM–SANS approach demonstrated in this study will provide a technical basis for an undertaking, leading to elucidation of the dynamic structures of functional IgG molecules that interact with antigens together with FcγR.

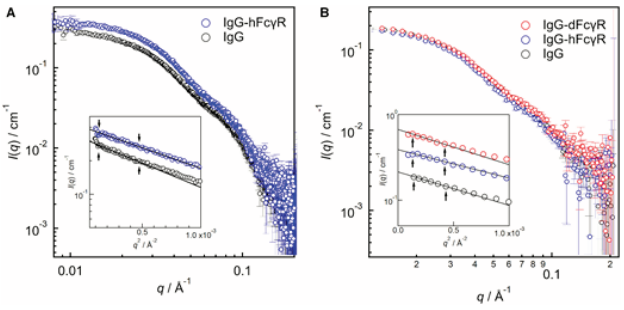

Fig. 2. (A) SEC–SAXS of IgG and IgG–hFcγR complex and (B) SEC–SANS profiles of IgG and IgG–hFcγR and IgG–dFcγR complexes. Guinier plots are shown in the insets in which the small arrows indicate fitting ranges.

REFERENCES:

[1] N. Sato *et al.*, *J. Biochem*, in press (2021). DOI: 10.1093/jb/mvab012

CO6-5 Structural characterization of circadian clock potein complexes

H. Yagi[1], Y. Yunoki[1,2], K. Morishima[3], A. Matsumoto[4], N. Sato[3], L. Porcar[5], A. Martel[5], R. Inoue[3], H. Kono[4], M. Sugiyama[3] and K. Kato[1,2]

[1]*Graduate School of Pharmaceutical Sciences, Nagoya City University*
[2]*Exploratory Research Center on Life and Living Systems, National Institutes of Natural Sciences*
[3]*Institute for Integrated Radiation and Nuclear Science, Kyoto University*
[4]*National Institutes for Quantum and Radiological Science and Technology*
[5]*Institut Laue-Langevin*

INTRODUCTION: The molecular machinery of the cyanobacterial circadian clock comprises three proteins: KaiA, KaiB, and KaiC. Through interactions among the three Kai proteins, the phosphorylation states of KaiC generate circadian oscillations *in vitro* in the presence of adenosine triphosphate (ATP). We especially focused on the KaiA-KaiB-KaiC ternary complex (ABC complex), which is considered to play the key role of the negative feedback loop of circadian rhythm. Recently, the cryo-electron microscopy (EM) structure of the ABC complex has been reported. However, the N-domains of KaiA subunits were poorly resolved due to their missing electron density maps. This observation probably reflected a high flexibility of linker between N- and C-domains. The whole structure of ABC complex has remained to be elucidated. Herein, for characterization of the overall structure of ABC complex, we conducted integrative techniques using small-angle X-ray scattering (SAXS), inverse contrast-matching small-angle neutron scattering (iCM-SANS), and native analytical ultracentrifugation (AUC) in conjunction with computer simulations.

EXPERIMENTS: The expression and purification of clock proteins, KaiA, KaiB and KaiC were performed according to methods previously described [1]. X-rays from a high-brilliance point-focused X-ray generator (MicroMAX-007HF, Rigaku, Tokyo, Japan) were focused with a confocal mirror (OptiSAXS) and collimated with a confocal multilayer mirror and two pinholes collimation system with the lower parasitic scattering, "ClearPinhole". The scattered X-rays were detected with a two-dimensional semiconductor detector (HyPix-6000, Rigaku, Tokyo, Japan). The sample-to-detector distance and wavelength of X-ray used for present work was 1320 mm and 1.542 Å, respectively. For removal of unfavorable aggregates from the sample solution, the laboratory-based SEC-SAXS System (LA-SSS) was employed to measure the SAXS profile in the Q range (0.01 $Å^{-1}$–0.2$Å^{-1}$). The SANS experiments were performed using the D22 instrument installed at the Institut Laue-Langevin (ILL), Grenoble, France. The sample-to-detector distance and wavelength of neutron used for present work was 5600 mm and 6.0 Å, respectively. SEC-SANS system was also utilized for present work.

RESULTS: To date, we have been conducting structural analysis of the ABC complex, which plays a key role in generating negative feedback in the regulation of circadian rhythms. Specifically, by combining solution scattering methods such as SAXS and SANS with gel filtration chromatography, we have extracted the overall structure of the ABC complex. The structural information of KaiA in the complex have succeeded in constructing structural models. In this year, the stability of the structural models was evaluated by molecular dynamics (MD) simulations. One hundred nsec MD simulations revealed that the N-domains of the 12 molecules of KaiA were highly mobile and there was little correlation of motion between the 12 molecules. The electron microscopic analysis of the ABC complex reported in the previous study assumed six-fold axial symmetry, and thus could not capture the structural information of the highly motile KaiA N-domain. Interestingly, the N-domains of KaiA cover the C-domains in one of stable ABC complex models (Fig. 1), which prevents KaiA from interacting with other KaiC molecules via its C-tail regions. In other words, KaiA changes its own conformation through the interaction with the KaiB-KaiC complex and negatively regulates the binding of other KaiC molecules in solution. Thus, the present study shows that the combination of solution scattering, computational modeling, and MD simulations enable us to construct a 3D structural model of the Kai protein complex, even in regions of high mobility.

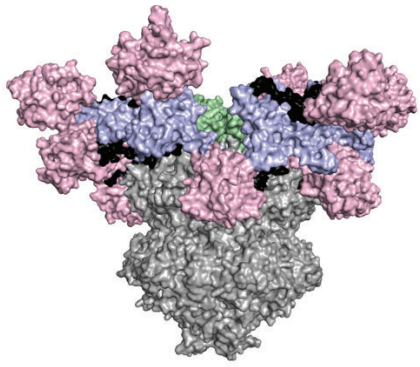

Fig. 1
A stable structural model of ABC complex evaluated by MD simulation.
N- and C-domains and linkers of KaiA, KaiB and KaiC are shown in pink, cyan, black, green and gray, respectively.

REFERENCES:
[1] M. Sugiyama *et al.*, Si. Rep., **6:35567 |** (2016).

CO6-6 Radioresistance Mechanisms Acquired by Adaptive Evolution and their Evolutionary Mechanisms

T. Saito

Institute for Integrated Radiation and Nuclear Science, Kyoto University

INTRODUCTION: In nature, organisms have evolved diversely by adapting themselves to various environmental conditions. Some organisms have been found to survive in extremely severe environments. Elucidating the mechanisms by which organisms adapt to severe environmental conditions can provide meaningful information regarding evolution and diversity. Some bacteria, known as radioresistant bacteria, demonstrate extreme resistance to ionizing radiation [1]. The mechanisms by which these bacteria resistant damage from to ionizing radiation is an interesting area of research on the adaptations employed by organisms in nature. In order to elucidate the mechanisms of radioresistance in these organisms, it is important to investigate their biological defense mechanisms against external stresses at the molecular level. However, studies conducted on radioresistant organisms in nature are particularly difficult due to limited knowledge of their genetic and biochemical properties. Therefore, in this study, radioresistant *Escherichia coli*, the wild-type genetic and biochemical characteristics of which have been elucidated in detail, were generated by an adaptive evolution experiment using gamma rays as the selective pressure, and the characteristics of the evolved radioresistant *E. coli* were compared to those of the wild-type. The generation of radioresistant *E. coli* with 7.9-fold resistance to gamma radiation compared to wild-type *E. coli* has been described in a previous report of this study [2]. In this report, the differences in gene expression status between wild-type and radioresistant *E. coli* are described.

EXPERIMENTS: Extraction of total RNA and RNA sequencing : Total RNA was extracted from *E. coli* cells using RNAiso Plus (Takara) and further purified using NucleoSpin RNA Clean-up XS (Macherey-Nagel). The quality of the resulting total RNA was evaluated and confirmed using the Agilent 2200 TapeStation (Agilent). rRNA was removed from total RNA using Ribo-Zero Magnetic Kit (Gram-Negative Bacteria) (Illumina). The sequence library was prepared from the resulting RNA using TruSeq Stranded mRNA Sample Prep Kit (Illumina). The quality of the sequence library was evaluated and confirmed using the Agilent 2100 Bioanalyzer (Agilent). Sequence analysis was performed using the NovaSeq 6000 (Illumina), NovaSeq 6000 S4 Reagent Kit (Illumina), and NovaSeq Xp 4-Lane Kit (Illumina). Gene expression levels were analyzed using the Genedata Profiler Genome (Genedata) and STAR [3]. All procedures were performed according to the manufacturer's instructions.

Analysis of gene expression status: In the analysis, gene expression data with “fragments per kilobase of exon per million reads mapped” values less than 1 for all samples from the two groups were filtered out to eliminate noise data. Genes differentially expressed in radioresistant *E. coli* compared to those in wild-type *E. coli* were identified by Welch's t-test and correction for multiple testing using the Benjamini and Hochberg method (BH method) [4]. In addition, Gene Ontology (GO) analysis for the differentially expressed genes (DEGs) in radioresistant *E. coli* was performed using the Database for Annotation, Visualization and Integrated Discovery bioinformatics resources ver.6.8.

Statistical analysis: Welch's t-test and BH method were used to identify DEGs among many genes, and a q-value of less than 0.05 was considered statistically significant. The Expression Analysis Systematic Explorer score was used to test for significance in the GO analysis, and a P-value of less than 0.05 was considered statistically significant [5].

RESULTS: The expression levels of 171 genes were significantly different in radioresistant *E. coli* than in wild-type *E. coli*. Among these genes, the expression levels of 115 genes were increased and 56 genes were decreased. GO analysis of genes highly expressed in radioresistant *E. coli* compared to wild-type *E. coli* showed that genes involved in SOS response, response to stimulus, DNA repair, and DNA metabolism were included in Annotation Cluster 1 with an Enrichment Score of 2.43. These results strongly suggest that the increased expression of genes involved in cell recovery, DNA repair, cell survival, and response to stress is involved in the high radioresistance mechanism in evolved radioresistant *E. coli*. In the future, more detailed studies are needed to understand how the increased expression of these genes is involved in the radioresistance mechanism of radioresistant *E. coli*.

REFERENCES:

[1] T. Saito, Viva Origino, **30** (2007) 85–92.
[2] T. Saito, KURNS ProgressReport 2019 (2020) 211.
[3] A. Dobin *et al.*, Bioinfomatics, **29** (2013) 15–21.
[4] Y. Benjamini and Y. Hochberg, J. R. Statist. Soc. B, **57** (1995) 289–300.
[5] D. W. Huang *et al.*, Nat. Protoc. **4** (2009) 44–57.

CO6-7 SAXS analysis of the formation process of the nucleation intermediate of insulin B chain: The measurement at different pH conditions

Y. Yoshikawa, N. Yamamoto[1], R. Inoue[2], M. Sugiyama[2], and E. Chatani

Graduate School of Science, Kobe University
[1]School of Medicine, Jichi Medical University
[2]Institute for Integrated Radiation and Nuclear Science, Kyoto University

INTRODUCTION: Amyloid fibrils are protein aggregates that are often associated with diseases. They are commonly characterized by β-sheet-rich structure and formed through nucleation and elongation steps. However, detailed mechanisms of protein association especially in the nucleation remain unclear.

In our previous work, we found that nucleation intermediates were formed in the early phases of amyloid formation of human insulin B chain [1]. This result suggested that early protein aggregation is sometimes involved in the nucleation process. In addition, our subsequent study showed that similar intermediate-mediated fibrillation occurs over a wide pH range of 5.2 to 9.1 [2]. Since the final amyloid fibril structure appears to vary with pH, it is worth investigating whether different types of intermediates are observed depending on pH.

In this study, we analyzed structural properties of the nucleation intermediates formed at pH5.2 by using small-angle X-ray scattering (SAXS). We previously measured time-resolved SAXS of the fibrillation reaction of insulin B chain at pH8.7, and it was found that the nucleation intermediate shows a rod-like shape and its size gradually increased during the formation (Yamamoto et al., submitted). By measuring the time course of the intermediate formation at pH 5.2 in comparison with that at pH 8.7, we discuss the structural property of the nucleation intermediate and furthermore, the effect of pH on the formation process.

EXPERIMENTS: B chain was prepared from human insulin as described previously [1]. The stock insulin B chain was diluted with 50 mM acetate buffer (pH5.2) at a concentration of 1.4 mg/ml. Immediately after the preparation, the sample solution was then put in a 1-mm path-length quartz cell. The SAXS pattern was collected at 25 °C with NANOPIX equipped with HyPix-6000 (Rigaku Corporation, Japan). A Cu K-α line (MicroMAX-007HF) was used as a beam source, which was further focused and collimated with a confocal multilayer mirror (OptiSAXS). Scattering data were collected continuously with an exposure time of 15 min. The camera length was set to 1.33 m and the range of the scattering vector q was from 0.0085 to 0.2 Å^{-1}.

RESULTS: Fig. 1 shows SAXS profiles of insulin B chain monitored at several time points in the process of the formation of the nucleation intermediate at pH5.2. Because the reaction speed was higher than that at pH8.7, only slight time-dependent change in the scattering profiles was observed. The slope of the log-log plot of was close to -1 within the time range of the measurement, from which we performed the analysis of a cross-section plot assuming that the shape of the peptide aggregates can be approximated as a rod.

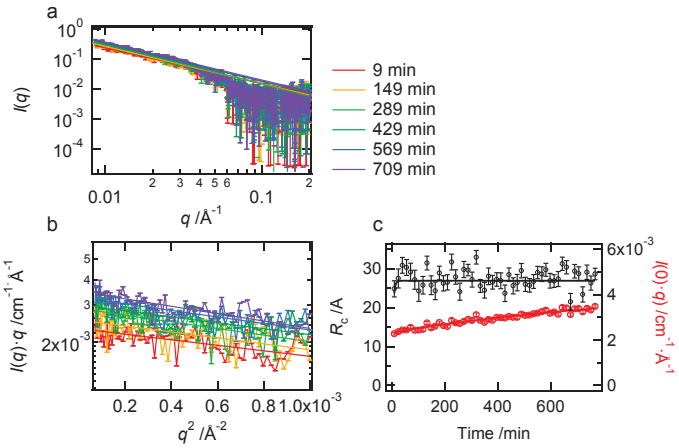

Fig. 1. (a) SAXS profiles of insulin B chain monitored at different time points. The lines indicate slopes obtained by line fit. (b) Cross-section plots of the profiles in panel (a). (c) Time dependence of the R_c (black) and the $I(0)\cdot q$ (red) values obtained from the cross-section plots.

We next performed the analysis of cross-section plot to obtain the radius (R_c) of the rod. Fig. 1b represents the plot and Fig. 1c shows the time dependence of R_c and the intercept ($I(0)\cdot q$) to represent the time dependency of the size development. The result suggested that the rod-shaped intermediates maintain the same radius. The radius of the rod (R_p), which is equal to $\sqrt{2}R_c$, was calculated to be 3.8±0.4 nm, and it was almost similar to that estimated at pH8.7 (3.6±0.1 nm). We further tried to estimate the length (L) of the rod based on Broersma's relationship using the R_p value and a diffusion coefficient obtained from a DLS measurement [2]. As a result, it is tentatively concluded that the basic size and shape of the nucleation intermediate at pH5.2 and pH8.7 are similar, although more detailed data analysis is necessary to lead the final conclusion. We are also planning to verify the similarity or difference of the nucleation intermediates formed at different pHs in terms of internal microscopic structure by using circular dichroism and other analytical techniques.

REFERENCES:

[1] N. Yamamoto *et al*., Sci. Rep., **8** (2018) 62.
[2] Y. Yoshikawa, Master Thesis, Kobe Univ. (2020).

CO6-8

Evaluation of boron neutron capture therapy (BNCT) using brain tumor bearing rats or mice models

Hideki Kashiwagi[1], Shinji Kawabata[1], Yusuke Fukuo[1], Takuya Kanemitsu[1], Koji Takeuchi[1], Gen Futamura[1], Ryo Hiramatsu[1], Hiroyuki Nakamura[2], Tsubasa Watanabe[3], Takushi Takata[3], Hiroki Tanaka[3], Minoru Suzuki[3], Shin-Ichi Miyatake[4], Koji Ono[4], Masahiko Wanibuchi[1]

[1] *Department of Neurosurgery, Osaka Medical and Pharmaceutical University*
[2] *Laboratory for Chemistry and Life Science, Institute of Innovative Research, Tokyo Institute of Technology*
[3] *Institute for Integrated Radiation and Nuclear Science, Kyoto University*
[4] *Kansai BNCT Medical Center, Osaka Medical and Pharmaceutical University*

INTRODUCTION:
Some BNCT clinical trials for glioblastoma have been conducted and have been showed the efficacy of BNCT for glioblastoma in our facility[1]. The development of new boron compounds for BNCT previously have been conducted all over the world in order to improve the effect of BNCT, however, there were no compounds to used clinical medicine except for BPA (boronophenylalanine) and BSH (borocaptate sodium). In this study, we focused on serum albumin, which is used for drug delivery. The serum albumin conjugate of a boron compound, maleimide-functionalized *closo*-dodecaborate albumin conjugate (MID-AC), has been developed by our group. We have previously found to be significantly inhibited the growth of tumor in a mouse colon 26 subcutaneous tumor model that received thermal neutron irradiation after MID-AC administration[2]. The therapeutic effect of MID-AC in BNCT for malignant gliomas was evaluated in this study.

Materials and Methods:
To evaluate the therapeutic effect of thermal neutron irradiation after MID-AC administration to F98 rat glioma models, an in vivo neutron irradiation experiment was performed at KUR. F98 rat glioma cells and Fischer rats were used and created F98 rat glioma models. The result was analyzed using Kaplan-Meier survival curves. The reactor power of KUR was 5 MW and the irradiation time was 20 minutes. The F98 rat glioma models were divided to 5 groups bellow: untreated control group (Untreated), neutron irradiated control group (Neutron only), neutron irradiation at 3 hours after BPA intravenous administration (i.v.) group (BNCT BPA), neutron irradiation at 3 hours after MID-AC i.v. group (BNCT MID-AC 3h), neutron irradiation at 24 hours after MID-AC i.v. group (BNCT MID-AC 24h).

RESULTS:
The result of neutron irradiation experiment was showed Table 1. below. The median survival times (MST) for each group were as follows: Untreated, 24.5 days〔95% confidence interval (CI); 23-27 days〕; Neutron only, 24.5 days〔95% CI; 23-27 days〕; BNCT BPA, 31.5 days〔95% CI; 28-40 days〕; BNCT MID-AC 3h, 33.5 days〔95% CI; 23-40 days〕; BNCT MID-AC 24h, 33.0 days〔95% CI; 27-36 days〕. MTS were prolonged significantly in the neutron irradiation group following boron compounds administration compared with Untreated (vs. BNCT BPA, $p < 0.0001$; vs. BNCT MID-AC 3h, $p = 0.0019$; vs. BNCT MID-AC 24h, $p = 0.0005$, respectively, log-rank test). MST were no significant differences in BNCT MID-AC 3h or 24h compared to BNCT BPA (vs. BNCT MID-AC 3h, $p = 0.94$; vs. BNCT MID-AC 24h, $p = 0.67$, respectively, log-rank test).

Table 1. The result of neutron irradiation experiment for the F98 rat glioma models

Group	n	MST (days)	95% CI (days)
Untreated	6	24.5	23-27
Neutron only	6	24.5	23-27
BNCT BPA	8	31.5	28-40
BNCT MID-AC 3h	8	33.5	23-40
BNCT MID-AC 24h	7	33.0	27-36

Ongoing research:
We have focused on folate acid (FA) and the folate receptor (FR) in addition to serum albumin. FA has a high affinity for FR, which are expressed to a limited extent in normal human tissues, but overexpressed in many cancer cells, including glioblastoma[3]. We have developed and evaluated PBC-IP, whose pteroyl group interacts with FR and has the ability to bind serum albumin. In vitro, PBCIP has been found higher cellular uptakes of boron in F98 rat glioma cells than BPA. The aim of the next study is to evaluate the therapeutic effect of PBC-IP on BNCT in the F98 rat glioma models.

REFERENCES:
[1] Kawabata, S., et al., Journal of Radiation Research, 2009. **50**(1): p. 51-60.
[2] Kikuchi, S., et al., J Control Release, 2016. **237**: p. 160-7.
[3] Nagai, T., et al., Cancer Immunol Immunother, 2009. **58**(10): p. 1577-86.

CO6-9

The study of boron neutron capture therapy (BNCT) for primary central nervous system lymphoma (PCNSL)

Hideki Kashiwagi[1], Shinji Kawabata[1], Yusuke Fukuo[1], Takuya Kanemitsu[1], Koji Takeuchi[1], Gen Futamura[1], Ryo Hiramatsu[1], Tsubasa Watanabe[2], Takushi Takata[2], Hiroki Tanaka[2], Minoru Suzuki[2], Shin-Ichi Miyatake[3], Koji Ono[3], Masahiko Wanibuchi[1]

[1] Department of Neurosurgery, Osaka Medical and Pharmaceutical University
[2] Institute for Integrated Radiation and Nuclear Science, Kyoto University
[3] Kansai BNCT Medical Center, Osaka Medical and Pharmaceutical University

INTRODUCTION:
Primary central nervous system lymphoma (PCNSL) is classified as a WHO Grade IV and accounts for 5% of all brain tumors[1]. The treatment for PCNSL is based on whole brain irradiation following high dose methotrexate (HD-MTX) chemotherapy. PCNSL is highly radiosensitive and the initial response rate is relatively high however the recurrence rate is high[2]. In the case of the recurrence additional irradiation is often difficult due to radiation damage. BNCT is considered to be an effective treatment for PCNSL recurrence because it is a highly cell-selective particle therapy. To expand the indications for PCNSL recurrence treatment, we conducted basic experiments of BNCT for PCNSL.

Materials and Methods:
A mouse PCNSL model was created using the Raji human lymphoma cell line, which has been shown to accumulate boron in tumor cells in vitro. In this model, the biodistribution was evaluated beforehand, and it was confirmed that the tumor-normal brain ratio was approximately 2 times. The boron compound used was boronophenylalanine (BPA), which was administered intraperitoneally and the dose was 500mg/kg body weight. The reactor power of the KUR was 5 MW and the irradiation times were 10 or 20 minutes. The models were randomly divided into the following 5 groups for neutron irradiation experiments: untreated control group (Untreated), neutron irradiation control group (Irrad.5MW 10min), neutron irradiation control group (Irrad.5MW 20min), BPA administration followed by neutron irradiation group (BPA 5MW 10min), and BPA administration followed by neutron irradiation group (BPA 5MW 20min). The results were analyzed using Kaplan-Meier survival curves.

RESULTS:
The PCNSL models were divided to 5 groups described above and the results were showed Table 1. below. The median survival times (MST) for each group were as follows: Untreated, 32.0 days〔95% confidence interval (CI); 27-45 days〕; Irrad.10min, 37.0 days〔95% CI; 25-60 days〕; Irrad.20min, 53.0 days〔95% CI; 25-78 days〕; BPA 10min, 30.0 days〔95% CI; 30-34 days〕; BPA 20min, 27.0 days〔95% CI; 27-29 days〕. The median survival times was significantly shorter in BPA 20min than in the Untreated ($p = 0.043 < 0.05$, log-rank test). The median survival time of Irrad.20min tends to be longer than Untreated ($p = 0.051$, log-rank test).

Table 1. The results of neutron irradiation experiments for the PCNSL models

Group	n	MST (days)	95% CI (days)
Untreated	6	32	27-45
Irrad.5MW 10min	6	37	25-60
Irrad.5MW 20min	6	53	25-78
BPA 5MW 10min	5	30	30-34
BPA 5MW 20min	6	27	27-29

Ongoing study:
In the PCNSL models using Raji lymphoma cells, the results of Kaplan-Meier survival curves of the neutron irradiation experiments predicted that the photon equivalent dose at 5MW 20min irradiation was the optimal dose. Early mortality in this study was considered to be due to acute oral mucosal damage caused by irradiation. Therefore, the predicted mucosal tissue doses were calculated assuming the compound biological effectiveness of BPA for oral mucosal tissues to be 4.9[3] and the boron concentration in mucosal tissue to be about 10 μg/g as measured in our laboratory; the photon equivalent dose of mucosa for BPA 5MW 10min was estimated to be about 10.9 Gy-Eq, and that for BPA 5MW 20min was about 17.8 Gy-Eq. When only the dose due to beam irradiation was calculated, the dose at Irrad.5MW 20min was about 3.9 Gy-Eq. We would like to use these dose results for dose adjustment in our next study and apply them to the treatment of the PCNSL models with BNCT using BPA.

REFERENCES:
[1] Neurol Med Chir (Tokyo), 2017. **57**(Suppl 1): p. 9-102.
[2] Nelson, D.F., et al., Int J Radiat Oncol Biol Phys, 1992. **23**(1): p. 9-17.
[3] Suzuki, M., et al., Journal of Radiation Research, 2014. **55**(1): p. 146-153.

CO6-10 Identification of amino acid residues responsible for the temperature dependency of sHsps from methanogens

M. Yohda, R. Midorikawa, K. Morishima[1], R. Inoue[1], M. Sugiyama[1]

Department of Biotechnology and Life Science, Tokyo University of Agriculture and Technology
[1]Institute for Integrated Radiation and Nuclear Science, Kyoto University

INTRODUCTION: Small heat-shock proteins (sHsps) are molecular chaperones ubiquitously present in all biological domains. It has a relatively conserved α-crystallin domain surrounded by variable N-terminal and C-terminal domains[1]. Each sHsp exists as a stable oligomer at around the optimum growth temperature of the organism. Oligomers dissociate into small oligomers under stress conditions such as high temperature to expose hydrophobic regions and capture denatured proteins to prevent aggregation. However, the temperature-dependent oligomer dissociation mechanism of sHsp has not been elucidated. Methanogenic archaea grow in a variety of environments. The optimum temperature of a hyperthemophilic one, *Methanocaldococcus jannaschii,* is 85°C. The sHsp of *M. jannaschii* (MJsHsp) exhibits high amino acid homology with that of the mesophilic *Methanococcus maripaludis,* which optimally grows at 38°C (MMsHsp). In this study, we tried to identify amino acid residues which determine the temperature dependency of sHsps from methanogens.

EXPERIMENTS: MJsHsp, MMsHsp, and their variants were expressed in *E. coli* using a pET23b vector. They were purified by anion exchange chromatography using TOYOPEARL DEAE-650, TOYOPEARL SuperQ-650 , and gel filtration chromatography using Superdex 200. The size of the oligomer structure under various temperature conditions was examined by size exclusion chromatography on HPLC (SEC), electron microscopy, and analytical ultracentrifugation (AUC). The chaperone activity was analyzed as the activity for protecting porcine heart citrate synthase from thermal aggregation.

RESULTS: In analytical ultracentrifuge, MJsHsp mainly existed as 24mer, which should correspond to the crystal structure[2]. Besides, larger oligomers were observed. MMsHsp also formed 24mer with partial dissociation into dimers (Fig. 1). This dissociation was concentration-dependent. The relative abundance of dimers increased at the lower the concentration. MJsHsp and MMsHsp) share significantly high amino acid sequence homology except for the N-terminus but differ greatly in temperature dependence. To verify whether the N-terminal domain determines temperature sensitivity, we created N-terminal exchange mutants and analyzed their temperature-dependent dissociation. However, it was revealed that the N-terminal domain is not related to temperature sensitivity. Then, we compared amino acid sequences of various methanogenic sHsps, and found a couple of amino acid replacements between hyperthermophilic sHsps and mesophilic ones. Two Gln residues at the N-terminus of the α-crystallin domain of MJsHsp (Q36, Q52) are changed to Glu in MMsHsp (E43, E59). The conserved C-terminal IXI motif of MJsHsp is INI (N145), and that of MMsHsp is IDI (D152). E118 of MJsHsp is changed to Gly in the mesophilic sHsps.

We constructed mutated sHsps and analyzed their temperature dependencies by gel filtration chromatography. Among various mutants of MMsHsp, MME43Q and MMD152N oligomers exhibited relatively high thermal stability (Fig. 2). Partial improvement in thermal stability was observed in the double mutant. However, the mutants were less stable than MJsHsp at the high temperature. MJsHsp did not show any change in temperature sensitivity for any of the mutants, leading to the conclusion that we cannot explain the temperature dependence by these mutants. The combination of various amino acid residues might be responsible for the temperature dependency.

Fig.1 AUC analyses of MJsHsp and MMsHsp

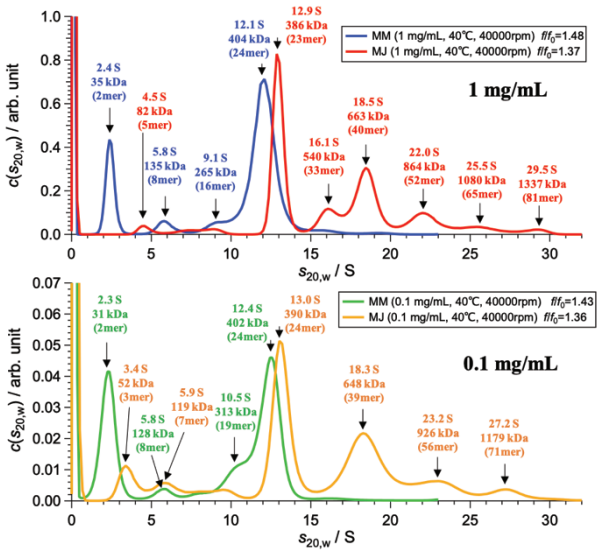

Fig. 2 Temperature dependency of MM variants

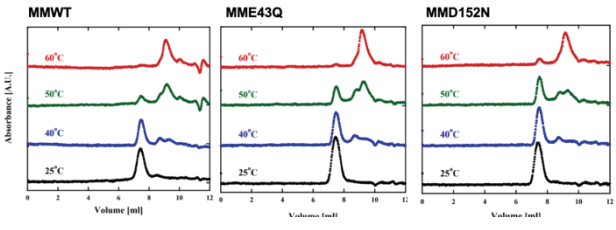

REFERENCES:

[1] C. Garrido *et al*., Int. J. Biochem. Cell Biol. **44** (2012) 1588–1592.
[2] K. K. Kim *et al*., Nature **394** (1998) 595–599.

CO6-11 Quantitative analysis of contribution of tumor vascular damage to antitumor effect of X-ray using BNCR

K. Ono[1], T. Watanabe[2], H. Tanaka[2], T. Takata[2], S. Suzuki[2]

[1]BNCT Joint Clinical Institute, Osaka Medical Pharmaceutical University
[2]Institute for Integrated Radiation and Nuclear Science, Kyoto University

NTRODUCTION: Tumor tissue consists of tumor cells and stroma, especially the vasculature that supplies the cells with oxygen and nutrients. The antitumor effect in BNCT is almost specific to cells accumulating boron compounds. In this study, we compare the effect of this tumor cell-specific BNCT with the effect of X-rays that has no tumor cell specificity, and quantitatively elucidate the effect of damage caused in the vascular system on the overall antitumor effect. This is the purpose of this research.

In fiscal 2020, we conducted an experiment to confirm the effect of BNCR on B-16 melanoma transplanted in C57-Black mice. This article reports the experimental results.

EXPERIMENTS: ***Mice, BPA administration and neutron irradiation.***

Mice: Eight-week-old C57-Black mice were prepared. The B-16 melanoma cells were transplanted to the right thigh, 10 days after then tumor grew to the size of average of 5mm.

BPA administration and measurement of ^{10}B concentration: ^{10}B-BPA in the form of a fructose complex (500 mg/kg body weight in terms of BPA) was administered subcutaneously in the posterior neck of mice. 30, 60 and 90 minutes after BPA injection, the tumors were removed and ^{10}B concentration was measured by using prompt γ-ray analysis.

Neutron irradiation: Based upon these concentration data (presented later), around 60 minutes after BPA injection, the neutrons were irradiated to the tumors in the thigh. The rest of the body was shielded with LiF plates. The highest neutron flux was 2.78×10^9/cm^{2}s. The flux was determined by the amount of activity induced in the gold foil.

Evaluation of radiation response.

In vivo evaluation by tumor growth delay: The tumor diameter of three directions was measured almost every 2 days by caliper. And tumor volume was calculated according to the following formula of π/6xabc.

In vitro colony formation assay: The tumor removed after neutron irradiation was minced by scissors, and digested with trypsin solution for about 15 minutes. After cell counting, an appropriate number of cells were plated onto the plastic petri dishes filled with fresh medium containing FCS. Twelve days later, the colonies were fixed with ethanol and stained with crystal violet. The numbers of colonies were counted by naked eye.

RESULTS and DISCUSSION:

^{10}B concentration with time after BPA injection.

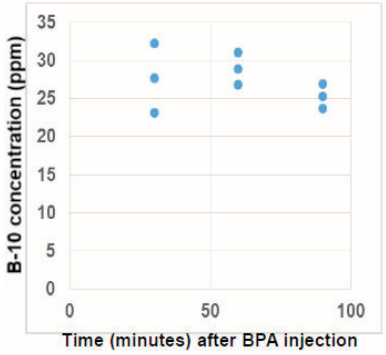

As presented in the figure, the ^{10}B concentration was around 28 ppm at 60 minutes. SUV (standerlized uptake value) was 1.1.

In vivo evaluation by tumor growth delay:

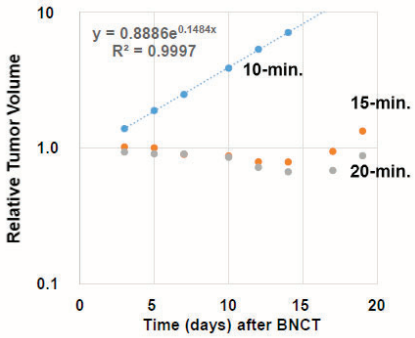

The effect of 10-minutes BNCT was quite small compared with 15, 20-minutes BNCT.

In vitro colony formation assay:

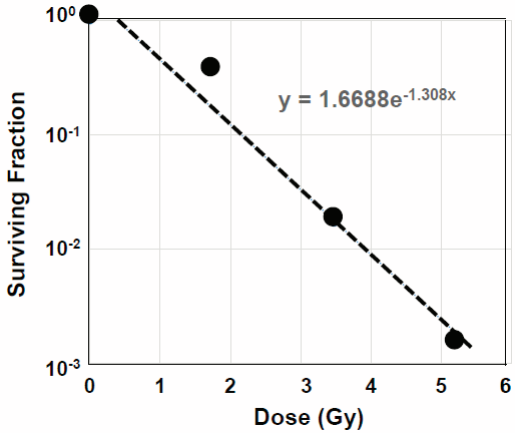

The result is a D_0 value of 0.765Gy to 0.846Gy. The value is in good agreement with the one estimated according to the formula established by K. Ono (2019 JRR).

CO6-12 ^{11}C medical-isotope production via the ^{12}C(γ,n)^{11}C reaction with carbon nano-tube (CNT)

N. Takahashi[1,2], M. Kurosawa[1], M. Tamura[1], M. Fujiwara[1],N. Abe[3], T. Kubota[3] and T. Takahashi[3]

[1]*Research Center for Nuclear Physics, Osaka University*
[2]*Kyoto Medical Technology Co., Ltd*
[3]*Institute for Integrated Radiation and Nuclear Science, Kyoto University*

INTRODUCTION: Nowadays, L-[^{11}C]-Methionine is widely recognized as a useful positron emission tomography (PET) reagents for the medical diagnosis of brain tumors [1]. The medical ^{11}C radioisotopes are most frequently produced in a cyclotron via the ^{14}N(p,α)^{11}C reaction by bombarding enriched nitrogen gas with a proton beam [2,3,4]. The produced ^{11}C radioactivities are mixed together with O_2 and target nitrogen gas. After some chemical processes under various controlled temperatures, the $^{11}CO_2$ is isolated from the target nitrogen gas [5]. Then, we can synthesize L-[^{11}C]-Methionine using the automated apparatuses. At present, Hokkaido University and Osaka University are actively working in collaboration, in order to obtain the formal government permission of the PET examination with L-[^{11}C]-Methionine for checking the metastasis and recurrence test of the brain tumor patient [6,7].

Apart from the cyclotron ^{11}C production, we studied a new method of the ^{11}C production using the bremsstrahlung γ-rays. There are important reasons for pursuing these kinds of investigations in series, since we have studied the medical isotope productions such as ^{99m}Tc, ^{18}F, ^{15}O isotopes via the photoreactions on natural Mo, Ne and O targets [8,9,10].

In the case of the ^{11}C production, we cannot use a ordinary ^{12}C target. Although the cross sections of the ^{12}C(γ,n)^{11}C reaction is very large, the specific activity of ^{11}C becomes very poor because of the number of ^{12}C in the target is extremely large. We cannot isolate the ^{11}C radioactivities from an enormous number of ^{12}C. Our idea to get the reasonable number of the ^{11}C specific activity, using the carbon nano-tube (CNT) as a target, instead of the ordinary carbon block or powder.

EXPERIMENTS: Figure 1 shows a carbon nano-tube (CNT) made of carbons strongly bonded together in a network with a diameter typically in a nanometer size. When the ^{12}C(γ,n)^{11}C reaction happens with incident high energy γ-rays, ^{11}C and neutron are released from the target nanotube. We introduce oxygen flow gas in the CNT powder target. The recoiled ^{11}C is captured by O_2 gas, making a $^{11}CO_2$ molecule. We prepare the O_2 gas circulation system, consisting mainly of 1) a CNT target with a nanotube powder isolated by two CNT sheets, 2) O_2 gas tubes, and 3) molecular sieves. We seal the CNT powders in the Al target vessel with the two CNT sheets for gas inlet and outlet. The O_2 gas flows through the CNT sheet and the CNT powders. We can trap the $^{11}CO_2$ using the molecular sieves. The ^{12}C(γ,n)^{11}C reaction experiment has been done using the bremsstrahlung γ-rays at the Linac facilty.

RESULTS: We confirmed that the $^{11}CO_2$ flowed out from the CNT target vessel through the CNT sheet by observing the 511 keV γ-rays at the molecular sieves. The measured decay curve of 511 keV γ-rays was well in agreement with the ^{11}C half-life of 20 minutes. The subjects remained are to determin the ^{11}C extraction efficiency from the CNT target and the specific activity with a ratio of ^{11}C/^{12}C. These work remained as future problems to be solved.

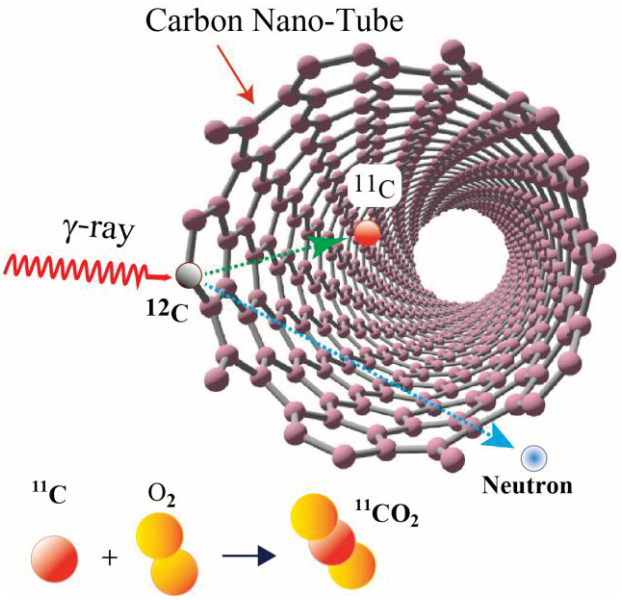

Fig. 1. Scheme of the ^{11}C medical-isotope production via the ^{12}C(γ,n)^{11}C reaction with the carbon nanotube (CNT). Neutron and ^{11}C are released from the strong bonding network of CNT after the ^{12}C(γ,n)^{11}C reaction following the nuclear two-body kinematics. Since the recoiled ^{11}C is chemically active, a $^{11}CO_2$ molecule is produced via the $^{11}C+O_2 \rightarrow {}^{11}CO_2$ chemical process.

REFERENCES:

[1] Y. Komatsu *et al.*, Radioisotopes, **67** (2018) 75-83.
[2] T.J. Ruth. A.P. Wolf, IEEE Trans., NS-**26** (1979) 1710.
[3] G.T. Bida et al., Radiochim. Acta., **27** (1979) 181.
[4] T.J. Ruth and M.J. Adam, Jornal of Radioanalytical and Nuclear Chemistry, **203** (1996) 457-469.
[5] M. Maziere *et al.*, Journal of Radioanalytical Chemistry, **56** (1980) 229-235.
[6] T. Nariai *et al.*, J. Neurosurg **103** (2005) 498-507.
[7] K. Isohashi *et al.*, EINMMI Resaerch **3** (2013) 27.
[8] T. Takeda *et al.*, Journal of Radioanalytical Chemistry, **318** (2018) 811-821.
[9] M. Kurosawa *et al.*, in preparation
[10] M. Fujiwara *et al.*, submitted to Journal of Radioanalytical Chemistry.

CO6-13

Demostrated Measuring by Laser Device of the Thickness of A Human Thigh Calcified Artery Vascular Tissue

N. Miyoshi and T. Takahashi[1]

Department of Gastroenterology/ Optical Clinic, Faculty of Medicine, Tsukuba University
[1] LINAC Beam-Line, Research Reactor Institute for Nuclear Science and Safety Nuclear Systems Research Center Accelerator Applied Engineering Research Field, Kyoto University

INTRODUCTION: The LINAC beam source in Kyoto University is unique one of higher purity and higher energy in the far infrared field. It is very sensitive spectroscopic measurements for the medical samples although the sample thickness is changes variously. It will be need to correct of the thickness effects. We tried the measurement them by the demonstrated measuring machine (Type CL-P.030) in this year (2020/30-31). As the thickness is proportional to the absorbance of a sample, the value of the absorbance is affected by dividing with the thickness to be corrected.

EXPERIMENTS: (1) Sample: A human thigh calcified artery vascular tissue was shown in Figure 1. **(2)** The mapping area of 4 lines (Z= 0, 1, 2, 3) are 14.7mm x 5mm x3 (220.5 mm^2) in Figure 1. **(3)** The laser device (Type CL-P030, Keyence Co., Osaka, Japan) was used to measure of the thickness of the sample in Figure 2.

RESULTS: [I] The area of 4 lines (Z=0, 1, 2, 3) was mapping of 14.7mm x 5mm x 3 (220.5 mm^2) through a human thigh calcified artery vascular tissue for 30 x 4 = 120 points as shown in Fig. 1.

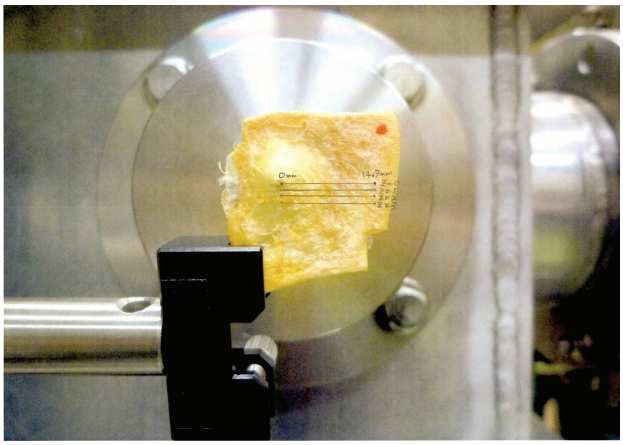

Fig.1: The mapping area of 4 lines (Z=0, 1, 2, 3) was 14.7mm x 5mm x3 (220.5 mm^2) of a human thigh calcified artery vascular tissue, respectively.

[II] The laser device was used for the demonstrated measuring of the sample thickness of the type of spot (minimum size: 38μm of diameter) as shown the performances in Fig.2.

Fig.2: The performance for the laser device of Type CLP030 (Spot-type: Right hand side) for the measurement of a sample thickness.

[III] The mapping measurement was automated drive on the sample stage by T. Takahashi.

[IV] The measured data were not so satisfied unstable as the thickness too sensitive, especially, transmitted lights at the demonstrated measurement. Detailed ingenuity will be required for the use it to develop of the thickness correction because the transmission will depend on the points of calcified or the normal vascular tissue.

The laser device instrument (Type CL-P030) was demonstrated from Keyence Co. and thanked for the demonstration to apply for the Basic Research A in the Grants-in-Aid for the Scientific Research on the last year (2020).

CO6-14 Design, Synthesis, and Evaluation of Glucose and Macrocyclic Polyamine-type Boron Carriers for NCT

S. Aoki[1,2], H. Ueda[1], M. Suzuki[3], Tanaka, T.[1] S. Masunaga[3], N. Kondo[3], and Y. Sakurai[3]

[1]*Faculty of Pharmaceutical Sciences, Tokyo University of Science*

[2]*Research Institute for Science and Technology, Tokyo University of Science*

[3]*KURNS*

INTRODUCTION: Boron neutron capture therapy (BNCT) is one of powerful therapies for local tumor control in the treatment of brain tumor, melanoma, and so on [1]. To date, only two boron-containing drugs, BSH (sodium mercaptoundecahydrododecaborate, $Na_2B_{12}H_{11}SH$) and L-4-boronophenylalanine (BPA) have been approved as clinically test compounds, and development of better BNCT agents is highly required.

We previously reported on the design and synthesis, of 2-boryl-1,2-dideoxy-D-glucose derivatives and other boryl-sugar analogs, although their intracellular uptake was not satisfying [2]. In this paper, we report on new phenylboronic acid-pendant macrocyclic polyamines **1~3** and their corresponding Zn^{2+} complexes **4~6** (Fig. 1).

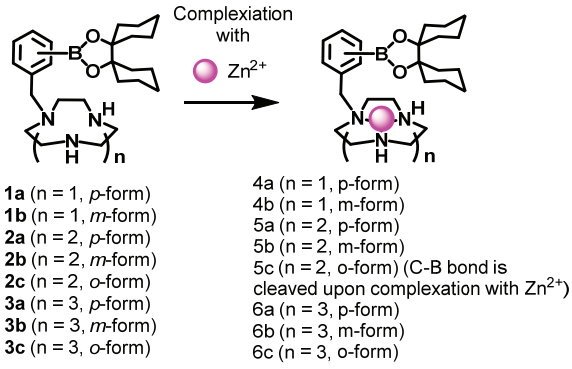

Fig. 1. Structures of boron-containing macrocyclic polyamines and the corresponding Zn^{2+} complexes

EXPERIMENTS and RESULTS: The synthesis of **1~3** and their Zn^{2+} complexes was carried out from s achieved according to our previous paper [3] and their cytotoxicity and cellular uptake activity against cancer cell lines (HeLa and A549 cells) and normal cell line (IMR-90) on ICP-MS (inductivity coupled plasma-mass spectrometer). As shown in Fig. 2., it was found that the intracellular uptake of **1~3 i**s higher than that of BSH and BPA, possibly due to the cationic charges of these molecules. The detailed study at low temperature and in the presence of specific inhibitors of the polyamine transporter system (PTS) suggest that the intracellular uptake of **1~3** is mediated by the clathrin-endocytosis pathway, possibly including PTS.

By comparison of the intracellular uptake, T/N (tumor/normal cell) ratios, and cytotoxicity of **1~3**, **1b**, **2b**, and **3a** were chosen as potent candidates for BNCT experiments. Because these molecules contained ^{10}B and ^{11}B in a natural abundance ratio ($^{10}B/^{11}B$ = 19.9/89.1), we synthesized the corresponding ^{10}B-enriched analogs, **^{10}B-1b**, **^{10}B-2b**, **^{10}B-3a** and their Zn^{2+} complexes **^{10}B-4b**, **^{10}B-5b**, **^{10}B-6a** *in situ* for BNCT experiments [4].

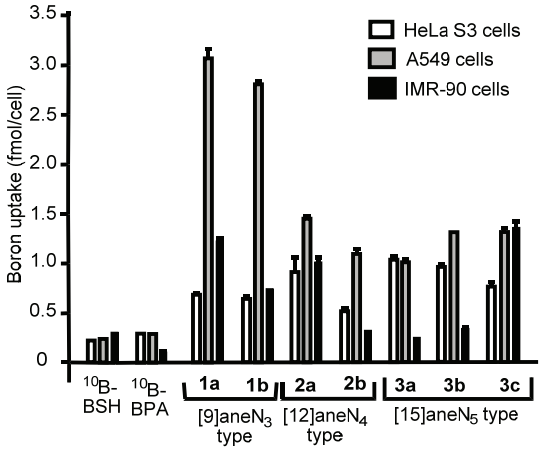

Fig. 2. The intracellular uptake **1~3** (30 μM) in HeLa S3 cells as determined on ICP-MS after the incubation with these drugs at 37 ºC for 24 hr. Data represent the mean ±SD of at least three replicates.

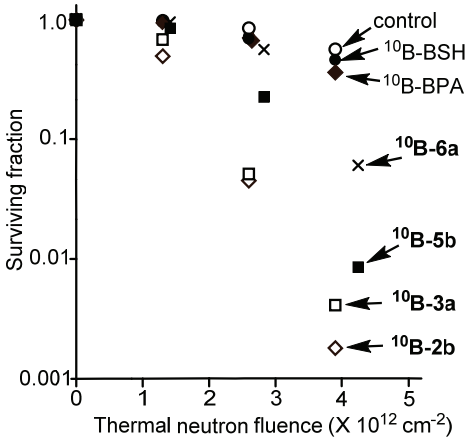

Fig. 3. Antitumor effect of ^{10}B-enriched BSH, BPA, **2b, 3a, 5b,** and **6a** (30 μM) against A549 cells upon irradiation with thermal neutron (averaged thermal neutron flux was 1.4 X 10^9 n/cm^2·s), as evaluated by a colony assay.

The results of BNCT of the these ^{10}B-enriched agents are summarized in Fig. 3, which indicates more potent BNCT effect of **^{10}B-2b**, **^{10}B-3a** **^{10}B-5b**, and **^{10}B-6a** than that of BSH and BPA [4]. The design and synthesis of boron carriers that have higher intracellular uptake and more potent BNCT effect are now in progress.

REFERENCES:

[1] a) R. F. Barth *et al.*, *Clin. Cancer Res.*, **11** (2005) 3987-4002. b) R. F. Barth et al. *Rad. Oncol*. **7** (2012) 146-166.

[2] T. Itoh, et al., *Bioorg. Med. Chem.* **26** (2018) 5922-5933.

[3] M. Kitamura, et al. *Inorg. Chem.* **50** (2011) 11568-11580.

[4] H. Ueda, et al. submitted for publication.

CO6-15 Preparation and Characterization of BPA-uridine conjugate for BNCT

K. Tanabe[1], M. Suzuki[2], and T. Nishihara[1]

[1]*Department of Chemistry and Biological Science, College of Science and Engineering, Aoyama Gakuin University*

[2]*Institute for Integrated Radiation and Nuclear Science, Kyoto University*

INTRODUCTION:

Modified nucleobases have been widely used as functional materials, and a variety of them have significant functions in biological systems. For example, 5-fluorouridine (5FU), 5-fluorodeoxyuridines (FdUrd) or cytarabine are well-known antitumor drugs and their derivatives act as stimuli-responsive prodrugs.[1] Thus, modified nucleobases are important as newly developed functional drugs.

In this study, we employed nucleobases as solubilizer of drugs for Boron Neutron Capture Therapy (BNCT) into aqueous solution as well as transport agent of drugs into the cells. We combined uridine and BPA and found that the resulting complex (BPA-uridine conjugate) smoothly dissolved in water. The cellular experiments revealed that BPA showed efficient cytotoxic effects in the presence of uridine and thermal neutron irradiation. Thus, uridine seems to be good agents for drug delivery system.

EXPERIMENTS:

Preparation of BPA-uridine conjugate. BPA was added to the aqueous solution of uridine and then the resulting mixture was heated to 80 °C for 6 h. After the BPA was dissolved in the solution, the mixture was cooled to room temperature to obtain BPA-uridine conjugate.

Cellular experiments using BPA and uridine in aqueous solution. The conjugate consisted of BPA (6 mM) and uridine was administered to the A549 cells and then the cells were incubated for 2 h. After incubation, the cells were irradiated (neutron, 1 MW) for 45 min at KUR. After incubation, WST 8 was added to the cells, and the cell viability assay was performed using Microplate Reader.

RESULTS:

Conventionally, fluctose has been used to solubilize BPA in water for the formation of their complex that showed hydrophilic properties. We expected that the uridine bearing ribose unit formed similar complex with BPA, and thus we combined BPA with uridine and prepared their conjugate. Eventually, we found that BPA-uridine conjugate was smoothly dissolved in water, and then applied them to cellular experiments.

For understanding of the biological activity of BPA in the presence of uridine, we measured the cytotoxicity of BPA-uridine conjugate against A549 cells, which were exposed to neutron (1 MW) in the presence of aqueous solution consisted of BPA and uridine and then incubated at 37 ˚C. Cell survival was determined by WST assay. Figure 1B and 1C compares cell survivals in the presence and absence of BPA-uridine after irradiation. The cytotoxic effect of radiation was significantly enhanced when the cells were irradiated in the presence of BPA-uridine. It is likely that BPA is effectively activated in the cells and thereby exhibits high cytotoxicity against tumor cells upon irradiation. In a separate experiment, we evaluated the cytotoxic effect of BPA in the presence of fluctose that complexed with BPA to dissolve into water. The cytotoxic assay revealed that BPA-fluctose conjugate showed similar cyototoxic effect upon irradiation. Thus, it is reasonable to conclude that BPA-uridine conjugate is a potent candidate agents for BNCT. In vivo experiments to evaluate the function of BPA-uridine is in progress.

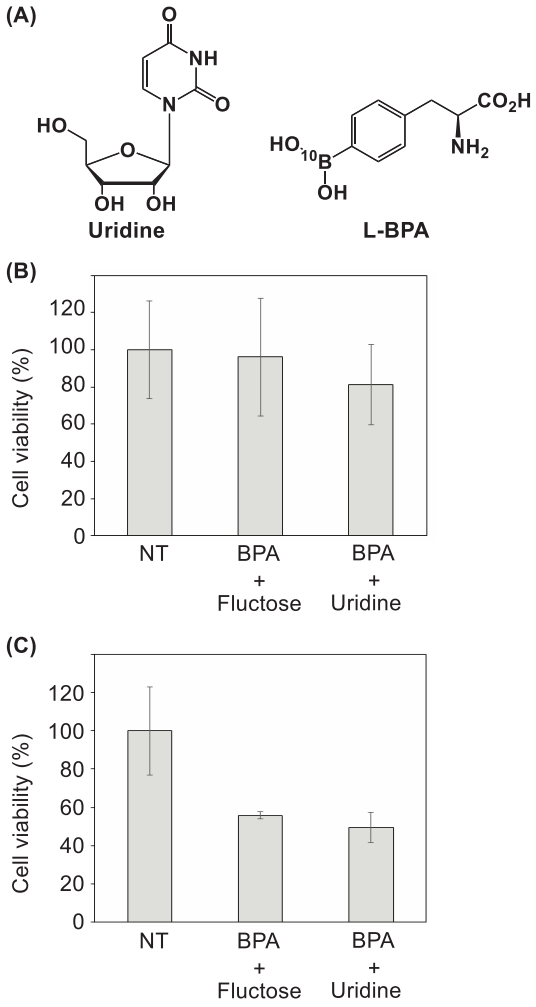

Figure 1. (A) Chemical structures of uridine and BPA. (B, C) Cytotoxic effect of BPA-uridine conjugate or BPA-fluctose conjugate upon ODN 1 upon thermal neutron irradiation (1 MW, 45 min).

REFERENCES:

[1] K. Tanabe *et al.*, *Org. Biomol. Chem.* **7** (2009), 651–654.

CO6-16 Asp racemization/isomerization in shedding products of cell adhesion molecule 1 is potentially involved in the neurodegeneration induced by elevated pressure

A. Yoneshige[1], A. Ito[1] and T. Takata[2]

[1]*Department of Pathology, Kindai University*
[2]*KURNS*

INTRODUCTION: The elevation of internal pressure is often involved in neurodegeneration; intraocular and intraventricular pressure elevations over 20–30 cmH_2O cause glaucoma and hydrocephalus, respectively.
Previously, to investigate the mechanisms by which elevation of intraluminal pressure causes cell or tissue degeneration, we devised a novel two-chamber culture system that enabled us to subject cultured cells to low levels of water pressure (2-50 cmH_2O pressure load) [1,2]. We found that mouse primary neurons degenerated when the water pressure was above 30 cmH_2O, and that ectodomain shedding of synaptic cell adhesion molecule 1 (CADM1) increased in a water pressure-dependent manner [1]. We also discovered that the increase of intracellular product of CADM1 shedding (C-terminal fragment, CADM1-CTF) resulted in decreased neurite density with punctate localization of CADM1 suggesting its aggregation in neurites [1].
CADM1-CTF is rich in Asp residues neighbored by Ala residues, and the conversion of these amino acids to poly-Gly diminished its aggregation state. Since the racemization and isomerization of Asp residues contributes to aggregation of various proteins and it likely occurred when the neighboring residues are small [3,4], these insights led us to hypothesize an involvement of Asp racemization/isomerization in the neurodegeneration induced by internal pressure elevation.

EXPERIMENTS:
(1) Synthetic peptide of internal sequence of CADM1-CTF (GADDAADADTAIINAEGGQNNSEEK) was incubated at 50°C for 0-15 days and applied to LC-MS to identify Asp isomer-containing peptides.
(2) Mouse neuroblastoma cell line Neuro-2a cells with exogenously expressed CADM1-CTF were cultured under 50 cmH_2O and were prepared for LC-MS analysis.
(3) To mimic the human ocular hypertension, immortal mouse neuroretinal cell line RGC-5 cells, primary neuroretinal cells, and mouse retinal explant cultures were prepared to exsert water pressure on to cells or tissues.
(4) The retinae or optic nerves of DBA/2J mice, a glaucoma model with ocular hypertension, were collected and subjected to CADM1 immunoblot analysis.

RESULTS:
(1) In LC-MS analysis of CADM1-CTF synthetic peptide, multiple peaks were detected after 1 day at pH 6.0 or pH 7.0 indicating that Asp racemization/isomerization could be occurred at neutral pH.
(2) CADM1-CTF proteins in Neuro-2a cells were solubilized with water, Triton X-100 containing buffer, or SDS containing buffer after 3 days culture under 50 cmH_2O, and CADM1 immunoblot was carried out. CADM1-CTF protein yields (CADM1-CTF / total proteins) were in the order Triton X-100 > SDS > water, however, the peptide peak was not identified using with LC-MS. The optimal conditions for LC-MS analysis should be determined in future study.
(3) Under 50 cmH_2O in the two-chamber culture device, the number of primary neuroretinal cells remained unchanged for 3 days with intact neurites, while the number of differentiated RGC-5 cells decreased after 2 days with loss of neurites. Primary neuroretinal cells would be more suitable for studying the effects of pressure elevation than RGC-5 cells. In retinal explant cultures, since PI-positive necrotic cells have begun to appear after 3 days at atmospheric pressure, the cultured retinae were collected at 2 days in vitro. The number of TUNEL-positive apoptotic retinal ganglion cells and the degree of GFAP-positive gliosis were analyzed histologically. Those neurodegenerative features were reproduced experimentally in cultured retinae at 50 cmH_2O (Fig. 1). Future experiments exploring Asp isomer-containing fragments in these crude cell/tissue lysates are planned.
(4) The CADM1 shedding rates were not changed in DBA/2J retinae, regardless of intraocular pressure. Further studies are necessary to elucidate whether Asp racemization/isomerization take place in full length CADM1 and its effects on CADM1 solubility and distribution.

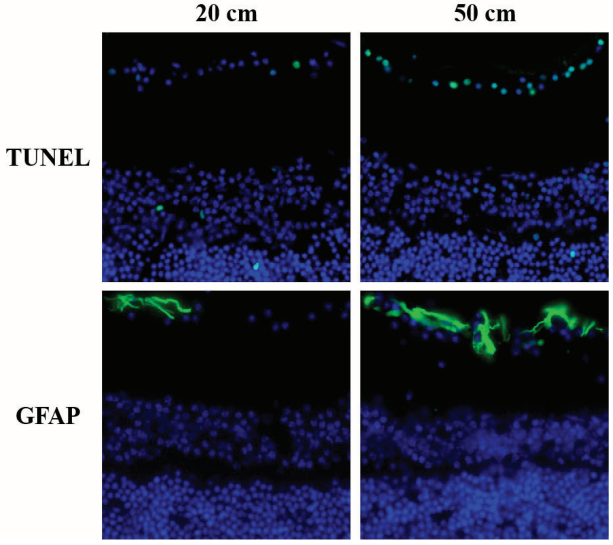

Fig. 1. Histological examinations of cultured retina with 2-50 cmH_2O pressure loading

REFERENCES:
[1] A. Yoneshige *et al.*, Mol. Neurobiol., **54** (2017) 6378-6390.
[2] M. Hagiyama *et al.*, Front. Physiol., **8** (2017) 997.
[3] N. Fujii *et al.*, J. Biochem., **116** (1994) 663-669.
[4] T. Takata *et al.*, Protein Sci., **29** (2020) 955-965.